

# Corrosion Behavior of Deep Water Oil Production Tubing Material Under Supercritical CO<sub>2</sub> Environment: Part 1—Effect of Pressure and Temperature

Yoon-Seok Choi,<sup>†\*</sup> Fernando Farelas,<sup>\*</sup> Srdjan Nešić,<sup>\*</sup> Alvaro Augusto O. Magalhães,<sup>\*\*</sup> and Cynthia de Azevedo Andrade<sup>\*\*</sup>

## ABSTRACT

The objective of the present study was to evaluate the corrosion properties of carbon steel in supercritical carbon dioxide (CO<sub>2</sub>)/brine mixtures related to the deep water oil production development. Corrosion tests were performed in 25 wt% sodium chloride (NaCl) solution under different CO<sub>2</sub> partial pressures (4, 8, 12 MPa) and temperatures (65°C, 90°C). Corrosion behavior of carbon steel was evaluated using electrochemical methods (linear polarization resistance [LPR] and electrochemical impedance spectroscopy [EIS]), weight-loss measurements, and surface analytical techniques (scanning electron microscopy [SEM], energy-dispersive x-ray spectroscopy [EDS], x-ray diffraction [XRD], and infinite focus microscopy [IFM]). The corrosion rates measured at 65°C showed a high corrosion rate (~10 mm/y) and a slight difference with pressure. Under these conditions, the sample surface was locally covered by iron carbide (Fe<sub>3</sub>C), which is porous and non-protective. However, the corrosion rates measured at 90°C increased with time at the initial period of the test and decreased to a very low value (~0.05 mm/y) due to the formation of protective iron carbonate (FeCO<sub>3</sub>) layer regardless the CO<sub>2</sub> partial pressure.

**KEY WORDS:** carbon steel, carbon dioxide corrosion, iron carbonate, supercritical carbon dioxide

## INTRODUCTION

Demand for energy in the world is fueling non-conventional oil discoveries such as deep water production; this brings many challenges that have necessitated engineering changes, design adaptations, and selection of alternative materials and systems.<sup>1-3</sup> A major issue in deep water production is corrosion and materials technology because of the extreme conditions (high pressure, high temperature, high carbon dioxide [CO<sub>2</sub>], and high chloride).<sup>4</sup> Even though the corrosion resistance alloy (CRA) has been available as a materials selection option for these severe environments, carbon and low-alloy steels are still widely used as tubing materials because of their strength, availability, and cost.<sup>5-7</sup>

The main difference between conventional oil production and deep water production is the reservoir pressure which exceeds 30 MPa often with significant amounts of CO<sub>2</sub>.<sup>1</sup> Consequently, the CO<sub>2</sub> might be in its supercritical state if the temperature and the pressure are over 31.1°C and 7.38 MPa, respectively. Based on the literature, it is known that the corrosion rate of carbon steel under supercritical CO<sub>2</sub> without protective iron carbonate (FeCO<sub>3</sub>) is very high (≥20 mm/y).<sup>8-12</sup> At certain conditions, the corrosion rate can decrease to low values (<1 mm/y) in long-term exposure as a result of the formation of a protective film of FeCO<sub>3</sub>.<sup>10-13</sup> Although studies related to general aqueous CO<sub>2</sub> corrosion at high CO<sub>2</sub> pressures have been carried out and reported recently, there are no comprehensive studies available for crude oil/CO<sub>2</sub>/brine environments at supercritical CO<sub>2</sub> conditions.

Submitted for publication: May 9, 2013. Revised and accepted: July 24, 2013. Preprint available online: August 6, 2013, doi: <http://dx.doi.org/10.5006/1019>.

<sup>†</sup> Corresponding author. E-mail: [choiy@ohio.edu](mailto:choiy@ohio.edu).

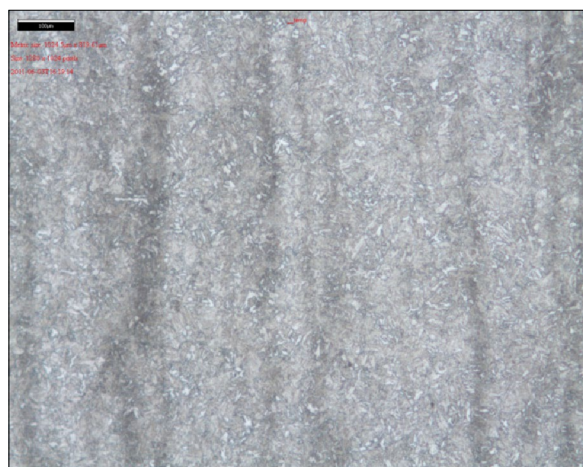
<sup>\*</sup> Institute for Corrosion and Multiphase Technology, Department of Chemical and Biomolecular Engineering, Ohio University, Athens, OH 45701.

<sup>\*\*</sup> Petrobras, Av. Horacio Macedo, 950 – Cidade Universitaria, Ilha do Fundao, Rio de Janeiro, RJ 21941-915, Brazil.

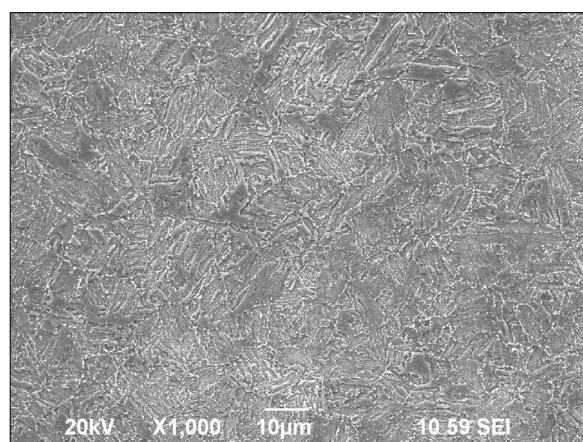
**TABLE 1**

Element Analysis by Atomic Emission Spectroscopy  
for the Carbon Steel (wt%)

C	Cr	Mn	P	S	Si	Fe
0.30	0.85	0.91	0.015	0.008	0.29	Bal.



(a)



(b)

**FIGURE 1.** Microstructure of the L80 carbon steel: (a) optical and (b) SEM images.

The overall objective of the study was to evaluate corrosion behavior of carbon steel in crude oil/supercritical CO<sub>2</sub>/brine mixtures related to the deep water oil production development. In the present study (Part 1), the corrosion properties of carbon steel were evaluated under different CO<sub>2</sub> partial pressures (4, 8, and 12 MPa) and temperatures (65°C and 90°C) in 25 wt% sodium chloride (NaCl) solution. The Part 2 study<sup>14</sup> strived to evaluate the corrosion behavior of carbon steel exposed to crude oil/supercritical CO<sub>2</sub>/brine mixtures at different water cuts (0, 30, 50, 70, and 100%) in a flowing 25 wt% NaCl solution.

<sup>(1)</sup> American Petroleum Institute (API), 1220 L St. NW, Washington, DC 20005.

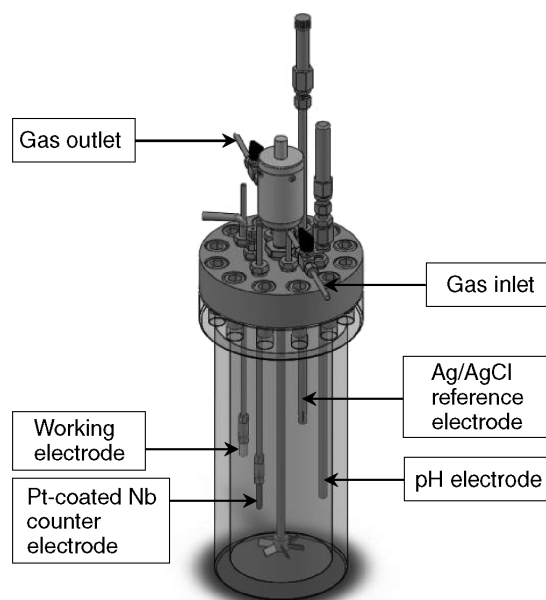


**FIGURE 2.** Schematic of autoclave system equipped for electrochemical measurements (stagnant condition without any agitation).

**TABLE 2**

Test Matrix for Corrosion Testing

Temperature (°C)	CO <sub>2</sub> pressure (MPa)		
	4	8	12
65	Gas phase	Supercritical phase	Supercritical phase
90	Gas phase	Supercritical phase	Supercritical phase

## EXPERIMENTAL PROCEDURES

The test specimens were machined from carbon steel (API<sup>(1)</sup> 5CT L80) with two different types: a rectangular type with a size of 1.27 cm by 1.27 cm by 0.254 cm for weight-loss measurement and surface analysis, and a cylinder type with 4.94 cm<sup>2</sup> exposed area for electrochemical measurements. The composition of steel is given in Table 1. Figure 1 shows the microstructure of the specimen, which presented typical tempered-martensite microstructure. Prior to exposure, the specimens were ground with 600-grit silicon carbide (SiC) paper, cleaned with isopropyl alcohol in an ultrasonic bath, and dried.

The corrosion experiments were carried out in a 4-L static stainless steel autoclave that contained a working electrode, a high-pressure/high-temperature silver/silver chloride (Ag/AgCl) reference electrode and a platinum-coated niobium counter electrode. Schematic of the autoclave with experimental setup is shown in Figure 2. All tests were conducted in 25 wt% NaCl aqueous solution. Table 2 shows the test conditions. During the experiment, corrosion rates were monitored with LPR and EIS measurements made at

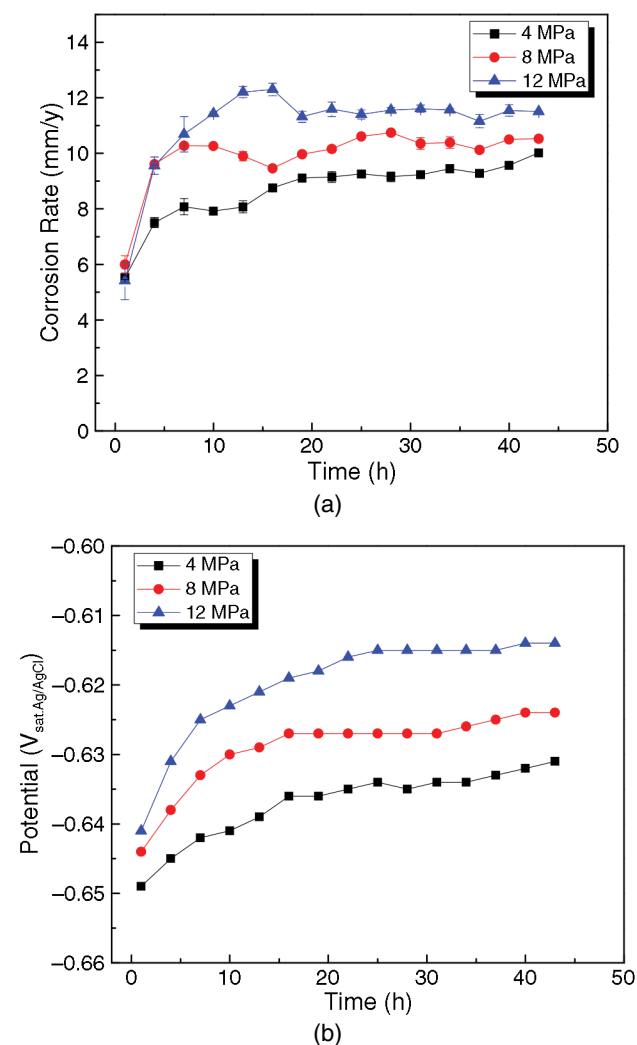


**FIGURE 3.** Variations of (a) corrosion rate and (b) corrosion potential with time for carbon steel with different CO<sub>2</sub> partial pressures at 65°C.

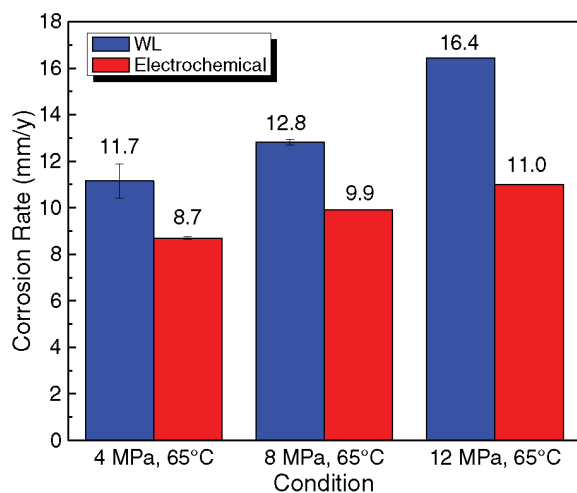


**FIGURE 4.** Comparison of corrosion rates obtained from weight-loss and electrochemical measurements (time-averaged) with different CO<sub>2</sub> partial pressures at 65°C for 48 h.

regular time intervals. LPR measurements were performed in a range of  $\pm 5$  mV with respect to the open-circuit potential (OCP) and a scan rate of 0.125 mV/s. Electrochemical impedance spectroscopy (EIS) measurements were conducted in the frequency range from 10 kHz to 10 mHz, with an alternating current (AC) signal amplitude of 5 mV (rms) at the OCP. The polarization resistance ( $R_p$ ), obtained from linear polarization resistance (LPR) and electrochemical impedance spectroscopy (EIS) techniques, was used to calculate the corrosion current density ( $i_{\text{corr}}$ ) using:

$$i_{\text{corr}} = \frac{B}{R_p} = \frac{\beta_a \times \beta_c}{2.3 \times R_p \times (\beta_a + \beta_c)} \quad (1)$$

where  $\beta_a$  is the anodic Tafel constant (40 mV/decade) and  $\beta_c$  is the cathodic Tafel constant (120 mV/decade). Then, the  $i_{\text{corr}}$  was converted into the corrosion rate:

$$\text{Corrosion rate (mm/y)} = \frac{0.00327 \times i_{\text{corr}} (\mu\text{A/cm}^2) \times \text{EW}}{\text{density (g/cm}^3)} \quad (2)$$

where EW is the equivalent weight in grams and 0.00327 is a constant factor used for dimension and time conversion.

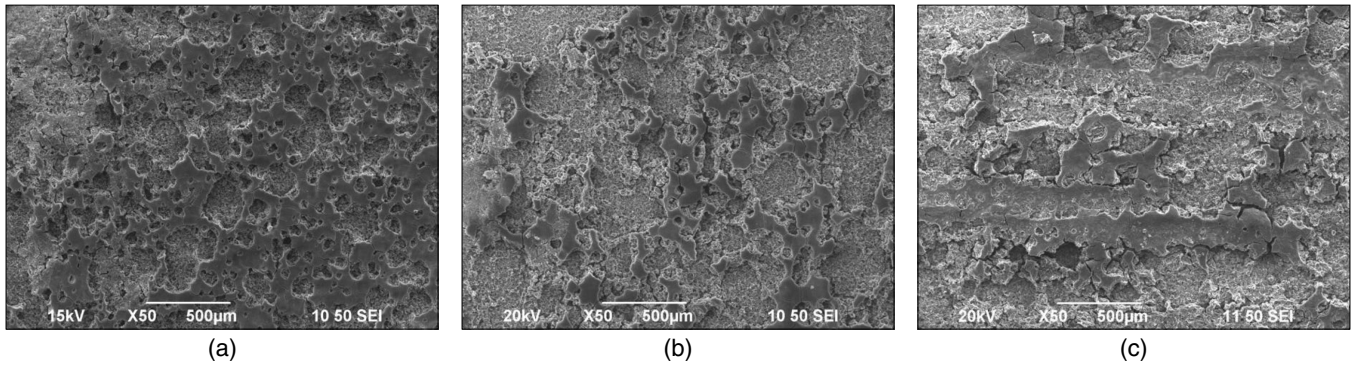
After the experiment, the specimen was taken through additional ex situ analyses. The morphology and compositions of corrosion products were analyzed using scanning electron microscopy (SEM), energy-dispersive spectroscopy (EDS), x-ray diffraction (XRD), and infinite focus microscopy (IFM).

## RESULTS AND DISCUSSION

### Experiments at 65°C

Figure 3 shows the variations of corrosion rate and OCP with time for carbon steel with different CO<sub>2</sub> partial pressures at 65°C. As shown in Figure 3(a), the initial corrosion rate was about 5.5 mm/y for all three conditions; it increased with time for approximately one day and then stayed constant after that. At the end of the test, the corrosion rates showed a slight difference in pressure, i.e., it showed a higher value at a higher pressure. This behavior can be attributed to the concentration of carbonic acid (H<sub>2</sub>CO<sub>3</sub>) in the brine. As the partial pressure of CO<sub>2</sub> increases, the concentration of H<sub>2</sub>CO<sub>3</sub> also increases, accelerating the cathodic reactions and therefore increasing the corrosion rate.<sup>9,15</sup> This can also be supported by the potential changes with time shown in Figure 3(b). A slightly more noble potential was measured for higher CO<sub>2</sub> partial pressure conditions, indicating a higher cathodic reaction rate.

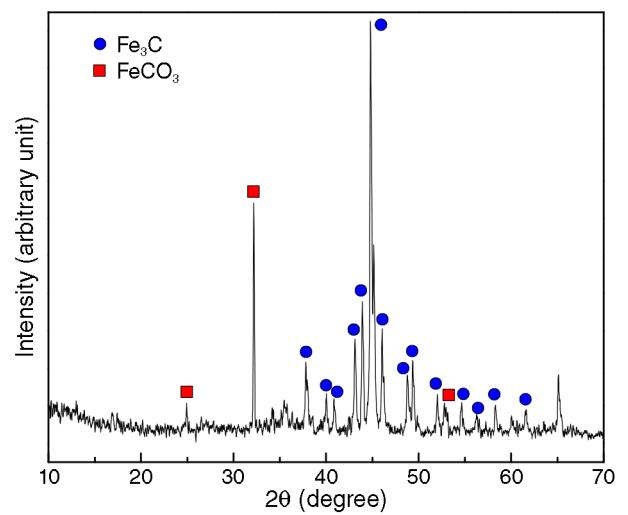
Figure 4 compares the average corrosion rate obtained from electrochemical (LPR) and weight-loss



**FIGURE 5.** SEM images of the corroded surface of the samples exposed to 25 wt% NaCl solution at 65°C: (a) 4 MPa, (b) 8 MPa, and (c) 12 MPa.

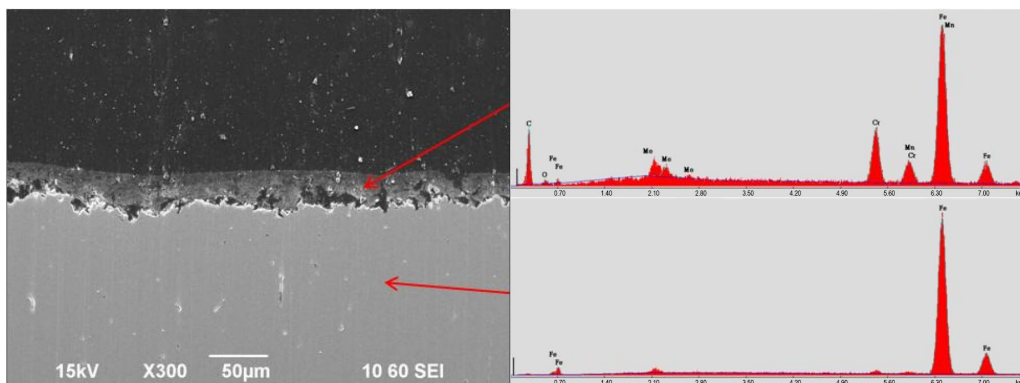
measurements under different CO<sub>2</sub> partial pressures. Under these experimental conditions, the corrosion rate measured by both techniques increased with pressure. The difference between them could be attributed to the approximate B value (13 mV) used for calculating the corrosion rate from the electrochemical measurements. In the present study, 13 mV of B value was used because it was assumed that reactions were governed by charge transfer under high-pressure CO<sub>2</sub> conditions. However, by comparing corrosion rates between LPR and weight-loss measurements, it is suggested that the real B value should be higher than 13 mV, indicating mixed control of charge transfer and mass transport.

Figure 5 shows the SEM images of the sample surfaces after 48 h of the exposure in the 25 wt% NaCl solution at 65°C with different CO<sub>2</sub> partial pressures (4, 8, and 12 MPa). It can be seen that the morphologies were almost identical for different pressures, and the surface was locally covered by the corrosion products. Figure 6 shows the XRD pattern of the corrosion product layer formed at 12 MPa, 65°C. The layer formed in this condition showed dominant iron carbide (Fe<sub>3</sub>C) diffraction patterns with some FeCO<sub>3</sub>. This indicated that the corrosion products shown in Figure 5 can be identified as Fe<sub>3</sub>C. The Fe<sub>3</sub>C



**FIGURE 6.** Result of XRD analysis for the sample exposed to 12 MPa, 65°C, for 48 h.

initially present in the carbon steel is exposed after the preferential dissolution of  $\alpha$ -Fe and accumulates on the steel surface; therefore, it is non-protective, porous, and easily spalls off from the steel substrate.<sup>16</sup> Figure 7 represents a cross-sectional SEM picture and EDS spectra of the sample exposed to 4 MPa CO<sub>2</sub> at



**FIGURE 7.** SEM image and EDS spectra of the cross section of the sample exposed to 4 MPa and 65°C for 48 h.

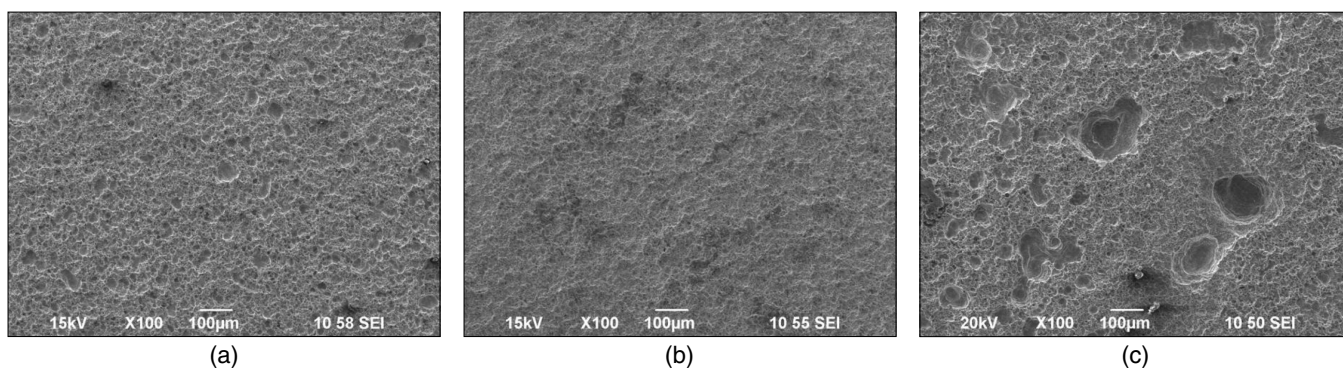


**FIGURE 8.** SEM images of the corroded surface of samples after cleaning: (a) 4 MPa, 65°C, (b) 8 MPa, 65°C, and (c) 12 MPa, 65°C.

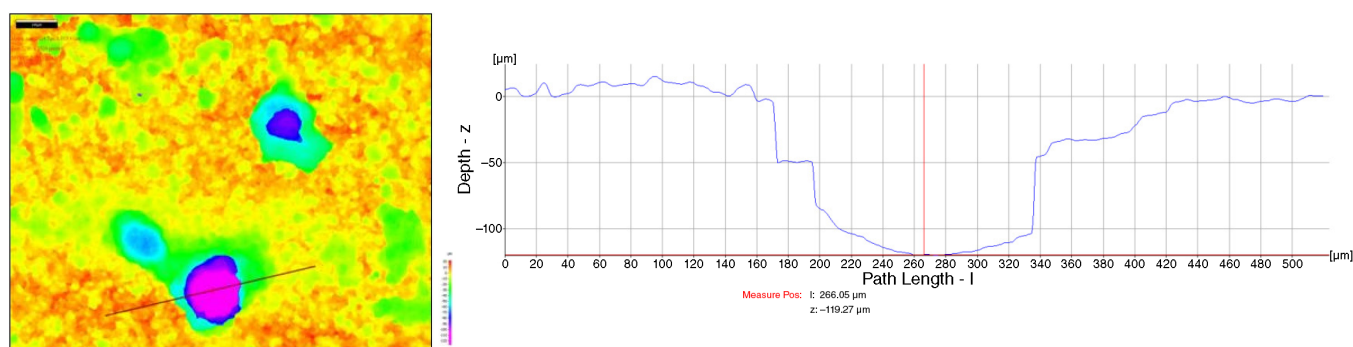


**FIGURE 9.** IFM surface analysis on the cleaned surface of the sample exposed to 12 MPa, 65°C, for 48 h.

**TABLE 3**

*Comparison of Corrosion Rates Obtained from Weight-Loss Measurements and Infinite Focus Microscopy Analysis at 65°C for 48 h*

	Corrosion Rate from Weight Loss (mm/y)	Maximum Pit Depth from IFM (µm)	Pit Penetration Rate (mm/y)
4 MPa	11.1	37.4	6.8
8 MPa	12.9	10.5	1.9
12 MPa	16.4	119.3	21.7

65°C. The presence of a porous  $\text{Fe}_3\text{C}$  layer on the steel surface with a thickness of approximately 27 µm is clearly observed.

Figure 8 shows the surface morphologies of samples after cleaning with Clarke's solution.<sup>17</sup> It can be seen that severe uniform corrosion attack was observed on the surface for samples at 4 MPa and 8 MPa, i.e., there was no localized corrosion. This implies that even though the  $\text{Fe}_3\text{C}$  layer locally formed on the steel surface, it did not initiate localized corrosion. However, in the case of 12 MPa, pits were observed on the cleaned surface, which may suggest localized corrosion under this condition. To measure a pit depth and calculate localized corrosion rate, IFM analysis was performed for all samples.

Figure 9 illustrates the result of IFM analysis for the sample that was exposed to 12 MPa  $\text{CO}_2$  partial pressure at 65°C. Additionally, Table 3 compares the corrosion rate obtained from weight-loss measurements and IFM analysis. In the particular cases of 4 MPa and 8 MPa, the pit penetration rate calculated from the maximum pit depth showed a lower value than the uniform corrosion rate, which confirms this corrosion type as uniform corrosion. At 12 MPa, the maximum pit depth was around 119 µm, which corresponds to a pit penetration rate of 21.7 mm/y. This rate is similar to the uniform corrosion rate obtained from the weight-loss measurement (16.4 mm/y), and this type of attack can be classified as severe uniform corrosion.

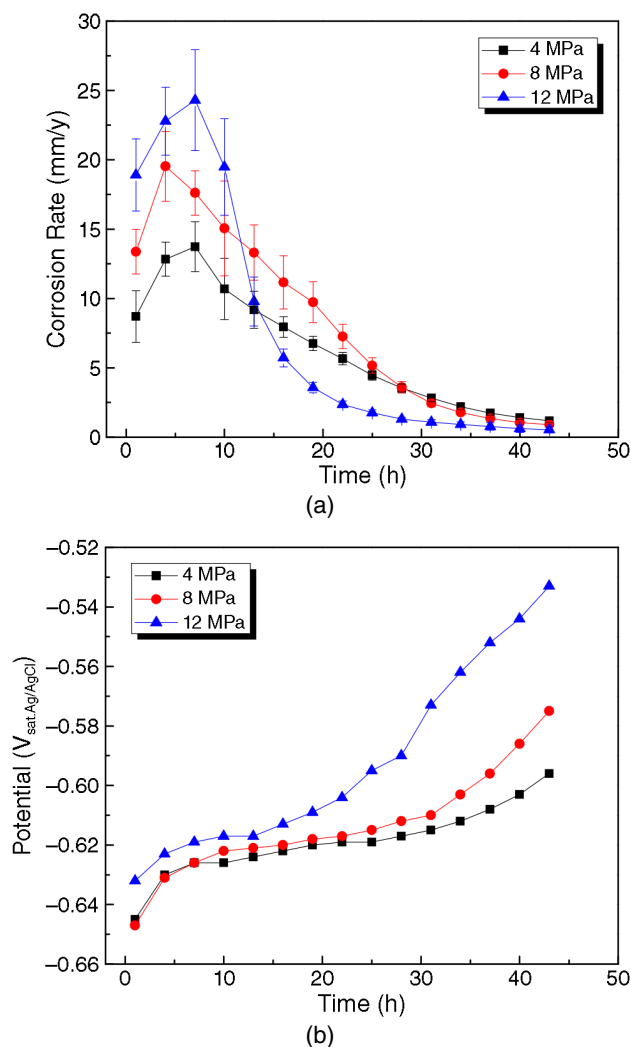


**FIGURE 10.** Variations of (a) corrosion rate and (b) corrosion potential with time for carbon steel with different CO<sub>2</sub> partial pressures at 90°C.

### Experiments at 90°C

Figure 10 shows the variations of corrosion rate and OCP with time for carbon steel at different CO<sub>2</sub> partial pressures exposed for 43 h at 90°C. At the beginning of the test, the corrosion rates increased for all three conditions. Higher corrosion rate was obtained for higher CO<sub>2</sub> partial pressure. Comparing the corrosion rates measured at 65°C and 90°C, the latter were much higher (almost double) during the first 7 h of exposure. Subsequently, a rapid decrease in the corrosion rates can be seen for all three conditions, reaching a low corrosion rate ( $\leq 1$  mm/y) at the end of 43 h of exposure.

The increase in corrosion rate at the initial periods of the test could be ascribed to the formation of the Fe<sub>3</sub>C layer on the steel surface. It has been proven that Fe<sub>3</sub>C is an electronic conductor so that its presence on the steel surface increases the corrosion rate by a galvanic effect between the steel substrate

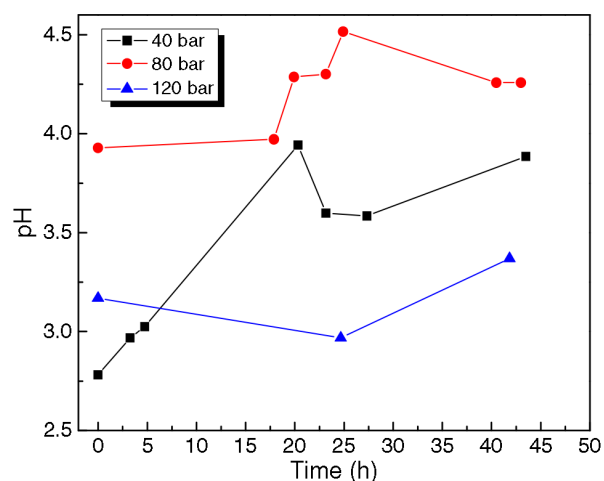


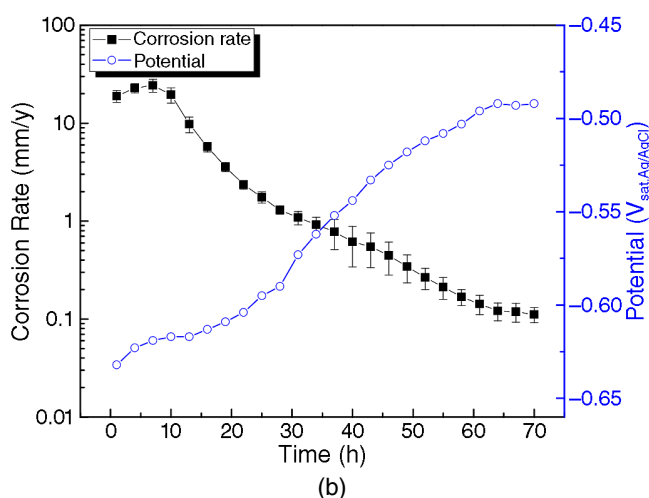
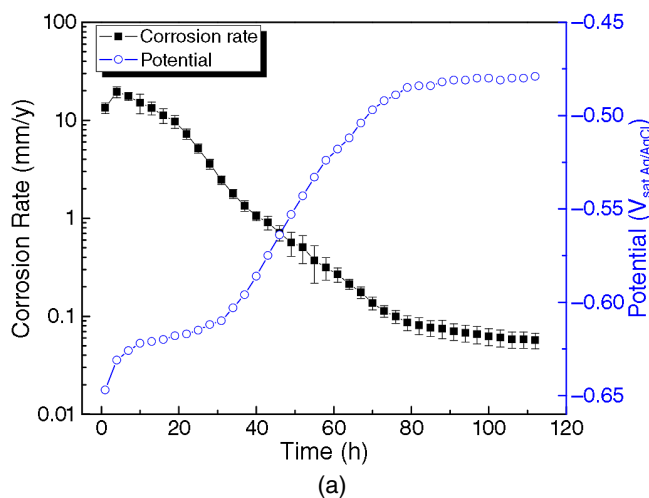
**FIGURE 11.** Variations of solution pH with different CO<sub>2</sub> partial pressures at 90°C.

and Fe<sub>3</sub>C layer.<sup>18</sup> Furthermore, the increase in corrosion rate with pressure is from an increase in the concentration of H<sub>2</sub>CO<sub>3</sub> in the solution as the partial pressure of CO<sub>2</sub> increases. The decrease in corrosion rates after 7 h can be attributed to the formation of a protective FeCO<sub>3</sub> layer. A more protective layer formed faster on the steel surface at higher CO<sub>2</sub> partial pressures. This is supported by a large shift in the corrosion potential toward more noble values at 12 MPa (Figure 10[b]).

Results of pH measurements are shown in Figure 11. The solution pH slightly changed during the test periods for all three conditions and showed 3.9 (40 bar), 4.3 (80 bar), and 3.4 (120 bar) at the end of the tests. However, there is no relationship between the corrosion rate and the solution pH for all conditions. This may be caused by the instability of zirconium dioxide (ZrO<sub>2</sub>)-based pH probe under high pressure and high temperature with high salt concentration.

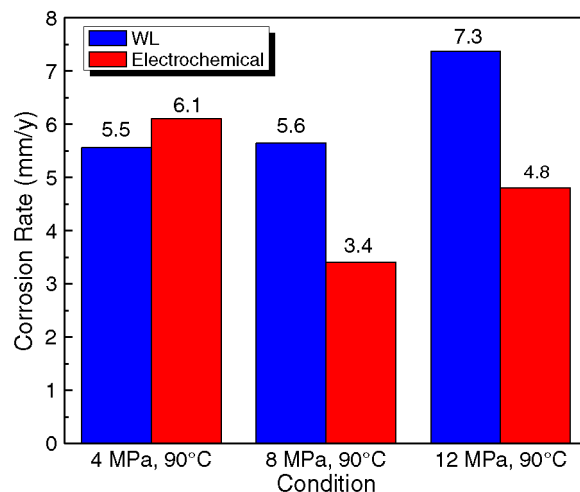
Since the corrosion rates kept decreasing at 43 h of exposure shown in Figure 10(a), experiments at 8 MPa and 12 MPa were continued until a stable corrosion rate was measured. Figure 12 shows the variations of corrosion rate and OCP for carbon steel with different CO<sub>2</sub> partial pressures at 90°C over an extended time. At 8 MPa the corrosion rate decreased up to 0.05 mm/y after 112 h of exposure, while at 12 MPa it decreased to 0.1 mm/y after 70 h of exposure. As a result of the formation of the protective FeCO<sub>3</sub> layer, the corrosion potential shifted to more noble values, and in both conditions a change of approximately 150 mV was observed.

Figure 13 compares the corrosion rates measured from weight-loss measurements and LPR measurements (average). The corrosion rates from both techniques showed high values compared with the final corrosion rates because of the high corrosion rates at the initial periods of the tests.



**FIGURE 12.** Variations of corrosion rate and corrosion potential with time for carbon steel with different  $\text{CO}_2$  partial pressures at  $90^\circ\text{C}$ : (a) 8 MPa and (b) 12 MPa.

SEM surface images of the samples are shown in Figure 14. It is interesting to note that for all three conditions, the surface does not appear to be fully covered by  $\text{FeCO}_3$ , even though very low corrosion rates were measured at 8 MPa and 12 MPa. However,



**FIGURE 13.** Comparison of corrosion rates obtained from weight-loss and electrochemical measurements (average) with different  $\text{CO}_2$  partial pressures at  $90^\circ\text{C}$  for 48 h (4 MPa), 114 h (8 MPa), and 72 h (12 MPa).

the true coverage by the protective  $\text{FeCO}_3$  layer can be properly judged only from cross-sectional images shown in Figures 16 through 18.

Figure 15 shows the XRD pattern of the corrosion product layers formed at 8 MPa,  $90^\circ\text{C}$  after 114 h. Although the surface does not appear to be fully covered by  $\text{FeCO}_3$  as shown in Figure 14(b), it showed only  $\text{FeCO}_3$  diffraction patterns.

Figures 16 through 18 represent the cross-sectional morphologies of the samples at different pressures. It can be seen from all three conditions that it has a “duplex” layer structure: an outer  $\text{Fe}_3\text{C}$  layer with some  $\text{FeCO}_3$  crystals and a thick/continuous inner  $\text{FeCO}_3$  layer underneath the  $\text{Fe}_3\text{C}$  layer, which was not seen in the tests at  $65^\circ\text{C}$ . In addition, a thicker inner  $\text{FeCO}_3$  layer formed at 8 MPa and 12 MPa than at 4 MPa because of the longer exposure time. Similar corrosion product morphologies have been observed recently under different experimental conditions.<sup>19-20</sup> Furthermore, it is known that the nucleation and growth of the inner  $\text{FeCO}_3$  typically starts at the steel

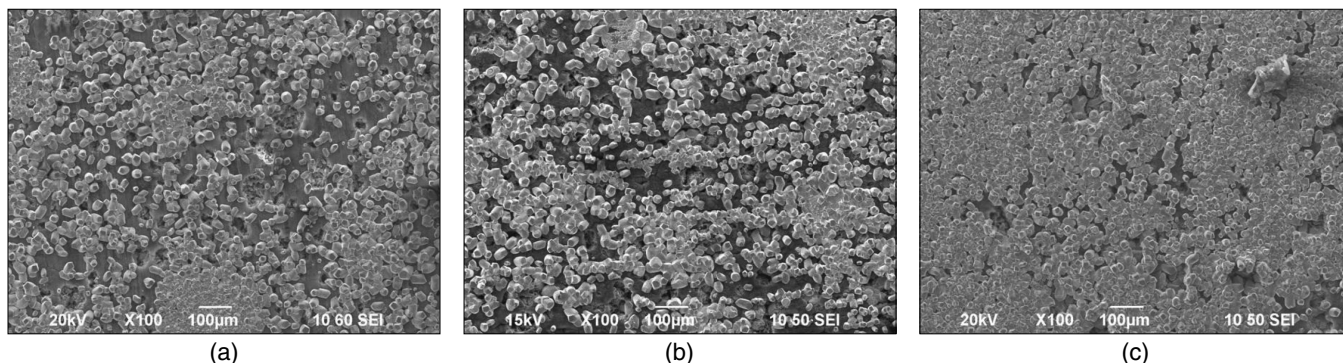


**FIGURE 14.** SEM images of the corroded surface of the sample exposed to a 25 wt% NaCl solution at  $90^\circ\text{C}$  for 48 h: (a) 4 MPa, (b) 8 MPa, and (c) 12 MPa.

surface because of the highest pH and  $\text{FeCO}_3$  saturation values achieved there.<sup>21</sup> This is because of the  $\text{Fe}_3\text{C}$  layer restricting the transport of acidic species in and ferrous ions out, so the most favorable conditions for the precipitation of a protective  $\text{FeCO}_3$  layer are found inside the porous  $\text{Fe}_3\text{C}$  layer at the steel interface. Furthermore, under stagnant conditions, high corrosion rates during the initial exposure could build up high concentrations of ferrous ion ( $\text{Fe}^{2+}$ ) at the steel surface. It is possible to have a surface pH that causes local saturation and enables the formation of  $\text{FeCO}_3$  on steel surface via precipitation, although the bulk solution pH is low, as shown in Figure 11. Therefore, the corrosion protection in the 90°C experiments was proven by the inner well attached and dense  $\text{FeCO}_3$  layer, which could not be seen from surface SEM observations, as shown in Figure 14.

Figure 19 shows the surface morphologies of samples after removing the corrosion product layer with Clarke's solution. Pits are observed for all conditions. To examine their depth and calculate pit penetration rate, IFM analysis was performed for all samples. Figure 20 shows results of the IFM analysis for samples exposed to different  $\text{CO}_2$  partial pressures at 90°C, and Table 4 compares the corrosion rate obtained from weight-loss measurements and IFM analysis. For all samples, the pit penetration rate calculated from the maximum pit depth showed higher values (2~3 times) than the time-averaged uniform corrosion rate, which suggests initiation of localized corrosion.

## CONCLUSIONS

- ❖ Uniform corrosion was observed at 65°C with a high corrosion rate (~10 mm/y) and little effect of  $\text{CO}_2$  partial pressure (at 4, 8, and 12 MPa). Under these conditions, the sample surface was locally covered by iron carbide ( $\text{Fe}_3\text{C}$ ), which is porous and non-protective.
- ❖ The corrosion rates measured at 90°C started out higher but ended up being very low ( $\leq 0.1$  mm/y) because of the formation of a protective  $\text{FeCO}_3$  layer, regardless the  $\text{CO}_2$  partial pressure. However, localized corrosion was seen with a maximum rate of 19 mm/y under this condition.

## REFERENCES

1. L.P. Ribeiro, C.A.S. Paulo, E.A. Neto, "Compos Basin-Subsea Equipment: Evolution and Next Steps," 2003 Offshore Technology Conf., paper no. 15223 (Richardson, TX: Offshore Technology Conference, 2003).
2. G. Estrella, "The Importance of Brazilian Deepwater Activities to the Oil Industry Technological Development," 2003 Offshore Technology Conf., paper no. 15049 (Richardson, TX: Offshore Technology Conference, 2003).
3. J.R.F. Moreira, P.S. Rovina, P. Couto, B. Neumann, "Development and Installation of the Drill Pipe Riser, An Innovative Deep-water Production and Completion/Workover Riser System," 1999 Offshore Technology Conf., paper no. 10892 (Richardson, TX: Offshore Technology Conference, 1999).

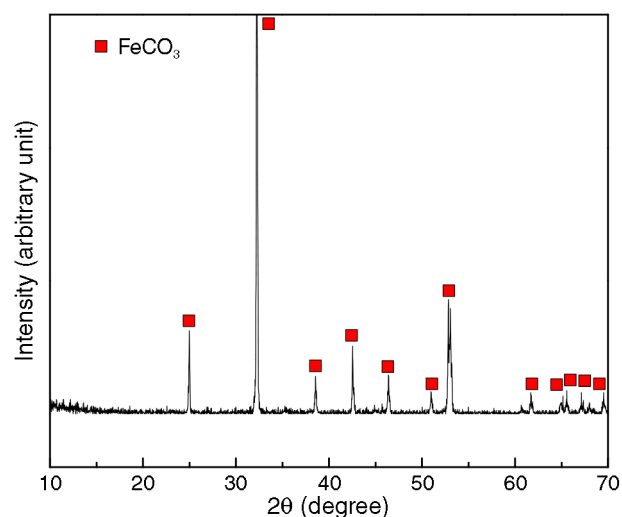


**FIGURE 15.** Result of XRD analysis for the sample exposed to 8 MPa, 90°C, for 114 h.

4. R.T. Hill, F.A. Ramirez, A.L. Perez, B.A. Monty, "Material Selection and Corrosion Control for Topside Process and Utility Piping and Equipment," CORROSION 2012, paper no. 1632 (Houston, TX: NACE International, 2012).
5. J. Carew, A. Al-Sayegh, A. Al-Hashem, "The Effect of Water-Cut on the Corrosion Behavior L80 Carbon Steel Under Downhole Conditions," CORROSION 2000, paper no. 00061 (Houston, TX: NACE, 2000).
6. J. Carew, A. Al-Hashem, "CO<sub>2</sub> Corrosion of L-80 Steel in Simulated Oil Well Conditions," CORROSION 2002, paper no. 02299 (Houston, TX: NACE, 2002).
7. H.J. Choi, D.K. Warnken, "Field Corrosion Assessment of L80 Carbon Steel Downhole Production Tubing in Khuff Gas Wells," CORROSION 2006, paper no. 06653 (Houston, TX: NACE, 2006).
8. Y.S. Choi, D. Young, S. Nešić, *Environ. Sci. Technol.* 44 (2010): p. 9233.
9. Y.S. Choi, S. Nešić, *Int. J. Greenhouse Gas Control* 5 (2011): p. 788.
10. Y. Zhang, X. Pang, S. Qu, X. Li, K. Gao, *Int. J. Greenhouse Gas Control* 5 (2011): p. 1643.
11. Y. Zhang, X. Pang, S. Qu, X. Li, K. Gao, *Corros. Sci.* 59 (2012): p. 186.
12. M.F. Suhor, M.F. Mohamed, A. Muhammad Nor, M. Singer, S. Nešić, "Corrosion of Mild Steel in High CO<sub>2</sub> Environment: Effect of the  $\text{FeCO}_3$  Layer," CORROSION 2012, paper no. 1434 (Houston, TX: NACE, 2012).
13. Z.D. Cui, S.L. Wu, S.L. Zhu, X.J. Yang, *Appl. Surf. Sci.* 252 (2006): p. 2368.
14. F. Farel, Y.S. Choi, S. Nešić, A.A.O. Magalhães, C. de Azevedo Andrade, "Corrosion Behavior of Deep Water Oil Production Tubing Material Under Supercritical CO<sub>2</sub> Environment: Part 2. Effect of Crude Oil and Flow," CORROSION 2013, paper no. 2381 (Houston, TX: NACE, 2013).
15. M.F. Mohamed, A.M. Nor, M.F. Suhor, M. Singer, Y.S. Choi, S. Nešić, "Water Chemistry for Corrosion Prediction in High Pressure CO<sub>2</sub> Environments," CORROSION 2011, paper no. 11375 (Houston, TX: NACE, 2011).
16. M.B. Kermani, A. Morshed, *Corrosion* 59 (2003): p. 659.
17. ASTM Standard G1-03, "Standard Practice for Preparing, Cleaning, and Evaluating Corrosion Test Specimens" (West Conshohocken, PA: ASTM International, 1999).
18. J. Crolet, N. Thevenot, S. Nešić, *Corrosion* 54 (1998): p. 194.
19. T. Berntsen, M. Seiersten, T. Hemmingsen, *Corrosion* 69 (2013): p. 601.
20. F. Farel, B. Brown, S. Nešić, "Iron Carbide and Its Influence on the Formation of Protective Iron Carbonate in CO<sub>2</sub> Corrosion of Mild Steel," CORROSION 2013, paper no. 2291 (Houston, TX: NACE, 2013).
21. F. Farel, M. Galicia, B. Brown, S. Nešić, H. Castaneda, *Corros. Sci.* 52 (2010): p. 509.

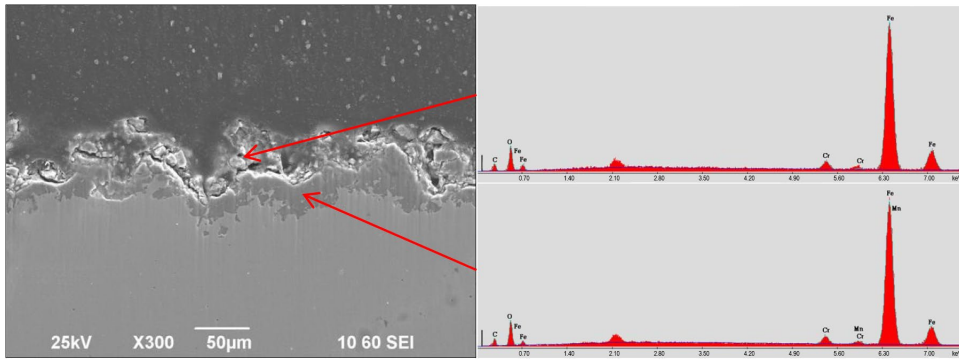


FIGURE 16. SEM image and EDS spectra of the cross section of the sample exposed to 4 MPa and 90°C for 48 h.

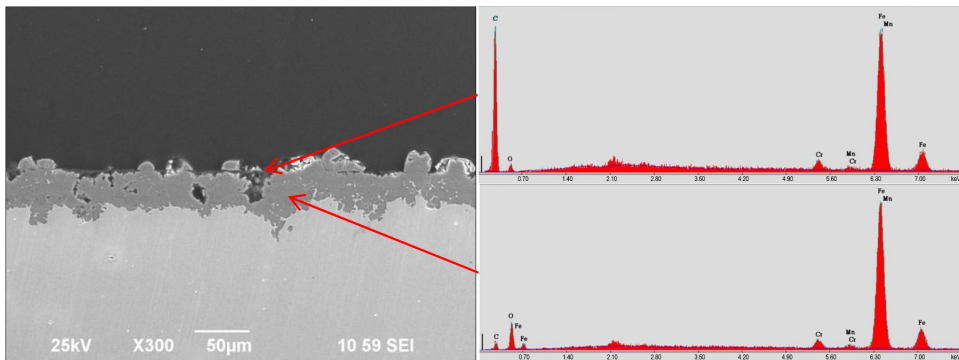


FIGURE 17. SEM image and EDS spectra of the cross section of the sample exposed to 8 MPa and 90°C for 114 h.

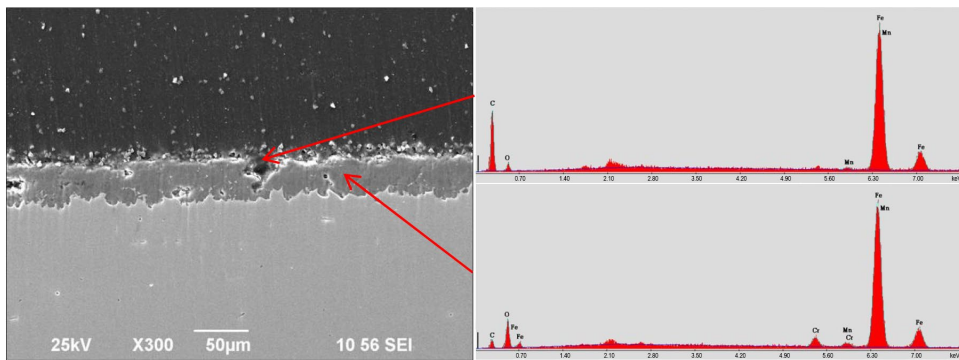


FIGURE 18. SEM image and EDS spectra of the cross section of the sample exposed to 12 MPa and 90°C for 72 h.

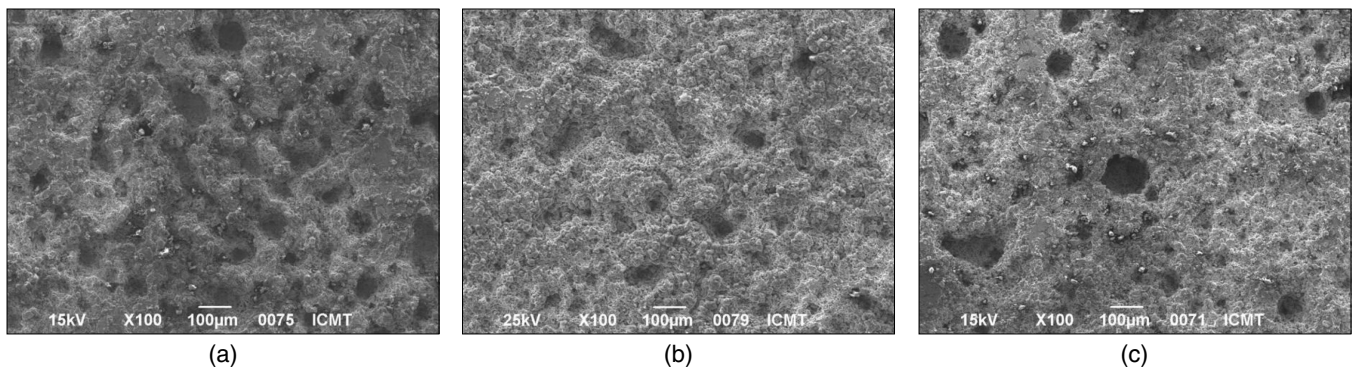
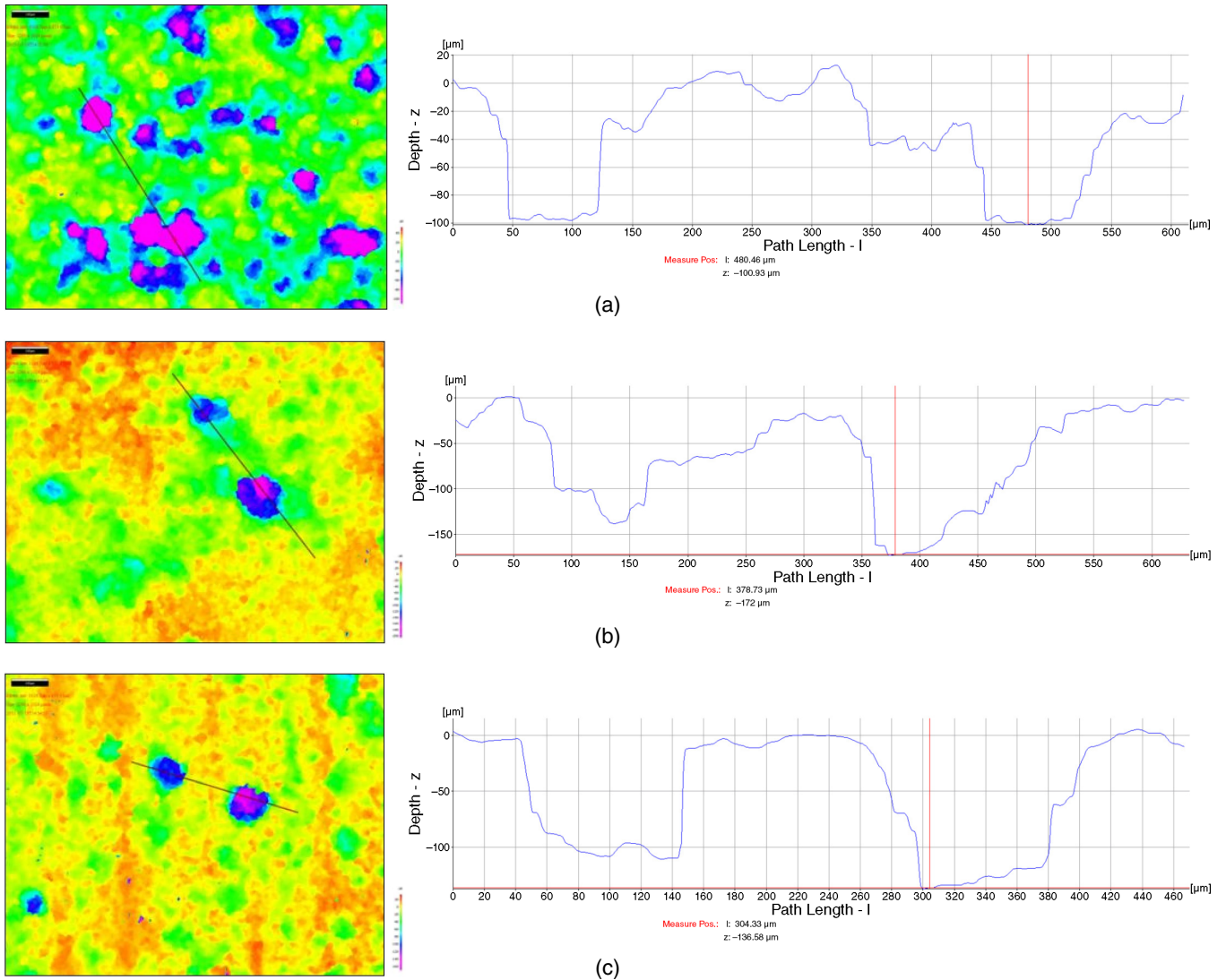


FIGURE 19. SEM images of the corroded surface of samples after cleaning: (a) 4 MPa, 90°C, (b) 8 MPa, 90°C, and (c) 12 MPa, 90°C.



**FIGURE 20.** IFM surface analysis on cleaned surface of the sample: (a) 4 MPa, 90°C, (b) 8 MPa, 90°C, (c) 12 MPa, 90°C.

**TABLE 4**

Comparison of Corrosion Rates Obtained from Weight-Loss Measurements and Infinite Focus Microscopy Analysis at 90°C<sup>(A)</sup>

	Corrosion Rate from Weight Loss (mm/y)	Maximum Pit Depth from IFM (μm)	Localized Corrosion Rate (mm/y)
4 MPa	5.5	100.9	18.4
8 MPa	5.6	172	13.2
12 MPa	7.3	136.5	16.6

<sup>(A)</sup> Exposure time: 48 h (4 MPa), 114 h (8 MPa), 72 h (12 MPa).